





Spatiotemporal dynamics of a modified Leslie–Gower predator–prey model: Effects of diffusion and taxis-driven movements on pattern formation

Anand Singh^{a,1} , Sayan Mandal^{b,2} , Pankaj Kumar Tiwari^b ,
Balram Dubey^a 

^aDepartment of Mathematics,
Birla Institute of Technology and Science Pilani,
Pilani, 333031, Rajasthan, India
anandsinghzhc@gmail.com; bdubey@pilani.bits-pilani.ac.in

^bDepartment of Basic Science and Humanities,
Indian Institute of Information Technology,
Bhagalpur, 813210, Bihar, India
sayanmandal321@gmail.com; pktiwari.math@iiitbh.ac.in

Received: February 23, 2025 / **Revised:** July 16, 2025 / **Published online:** October 10, 2025

Abstract. In this manuscript, we investigate a Leslie–Gower predator–prey model with Crowley–Martin-type functional response. We also explore the dynamics of reaction–diffusion as well as reaction–diffusion–advection model. Specifically, our study focuses on an ecological model involving a generalist predator that induces fear, has carry-over effects, and experiences competitive interference. For the temporal model, a detailed mathematical analysis is carried out, investigating the positivity and boundedness of the solutions. We observe both monostability and bistability phenomena, and explore various local and global bifurcations by varying the fear and carry-over parameters. Interestingly, the fear and its carry-over effects have opposing roles in influencing stability within the temporal model. We incorporated prey-taxis into a general reaction–diffusion framework to represent the directed movement of predators towards regions with higher prey densities or when tracking signals such as scent to locate their prey. We perform the complete analysis of diffusion-driven and taxis-driven instability for reaction–diffusion and reaction–diffusion–advection models, respectively. Our findings emphasize the significant influence of predator diffusion and prey-taxis on pattern formation, revealing that increased random predator movement, combined with a moderate level of prey-taxis, can stabilize the model.

Keywords: fear effect, carry-over effect, bifurcations, prey-taxis, Turing pattern.

¹The author was supported by a fellowship from BITS Pilani, Pilani Campus, India.

²The author was supported by a National Fellowship for Scheduled Caste Students [No. F. 40-2/June 2021 (CSIR NET Fellowship), Ref. No. 211610077551].

1 Introduction

Predator–prey dynamics remain a central focus of research in both ecology and evolutionary biology with mathematical models playing a key role in understanding their complexity. Within predator–prey systems, predation plays a vital role in species persistence, raising the fundamental question of how predators influence prey. Predators affect prey both directly, by hunting and killing them, and indirectly, by inducing behavioral and physiological changes through fear [1]. Fear can drive prey to adopt antipredator strategies such as increased vigilance, reduced foraging, avoidance of risky habitats, altered reproductive activity, and relocation to safer areas [15]. Experimental work on song sparrows (*Melospiza melodia*) by Zanette et al. [22] showed that predator fear altered nesting, feeding, and flight behaviors, reducing offspring production by 40%. Inspired by such evidence, Wang et al. [21] introduced the first mathematical model capturing the role of fear in prey dynamics, which was followed by many subsequent studies examining its impact on predator–prey models [5, 17].

The term “carry-over effects” stems from extensive clinical research and refers to how an organism’s previous experiences and history can affect its current performance [14]. On the flip side, these effects can become detrimental when high-quality habitats are lost. The degree and nature of population changes depend on (i) the demographic factors during specific periods causing significant carry-over effects and (ii) the quantity and the quality of the lost habitat. Experimental studies [4, 12] show that carry-over effects can arise within a single season across various species such as amphibians, insects, and marine invertebrates. Consequently, including carry-over effects in population models is essential for understanding potential connections between reproductive costs and life-history trade-offs.

Reaction–diffusion models have gained significant attention as a valuable tool for understanding the mechanisms underlying pattern formation. In such models, predators actively hunt prey, while prey attempt to escape, resulting in population density fluctuations across different spatial regions. The interplay between space and time drives population dynamics in response to the unpredictable movements of individuals. Various factors can influence organism movement, including the search for food, predator avoidance, or escaping high-risk areas for infection. The spatial distribution of organisms can lead to instability, known as Turing instability [20], which can cause the emergence of spatial patterns. Gierer and Meinhardt [6] developed a biological framework for a Turing model. Misra et al. [13] explored various spatiotemporal patterns in a cholera transmission model. Recently, extensive research has been done on exploring spatial patterns in spatiotemporal models [2, 5].

The word “taxis” is derived from the Greek term “taxis”, meaning arrangement. Taxis occurs when organisms adjust their movement patterns, known as kinesis, in response to a stimulus. Othmer et al. [19] defined taxis as either positive or negative, depending on whether the movement is directed toward or away from the external stimulus influencing the movement. In this way, taxis can be seen as random motion with a directional bias, while kinesis refers to random motion with a spatial bias. Lee et al. [9] investigated the key conditions necessary for pattern formation in prey-taxis models. The advection term

encapsulates the dynamics of predator locomotion predicated on the hypothesis of prey-taxis, wherein the acceleration of predators is directly related to the gradient of prey density. The mechanism of predation is conceptualized as an amalgamation of stochastic movement, facilitated by diffusion, and purposeful movement, driven by prey-taxis. In plankton populations, random movement at different velocities can lead to spatial pattern formation [11], while the directed movement of zooplankton, driven by their foraging behavior toward areas with high phytoplankton density, plays a role in pattern formation in plankton community models [10].

Based on the literature reviewed, we propose a prey-generalist predator model that integrates competitive interference, predator-induced fear along with its carry-over effects, constant prey refuge, self-diffusion, prey-taxis, and predator velocity. To the best of the authors' knowledge, a model with this combination of factors has not been previously developed. In this article, our goal is to accomplish the following research objectives:

1. Analyze how predator-induced fear and its carry-over effects along with constant prey refuge influence the dynamics of both prey and predator populations.
2. Investigate how predator diffusion affects the random movement of species.
3. Evaluate the role of prey-taxis in shaping the directed movement of species toward or away from prey density gradients.

The structure of this paper is outlined as follows: Section 2 introduces the primary ecological model, incorporating predator-induced fear, its carry-over effects, and diffusion terms. A predator–prey model with prey-taxis is developed to represent these dynamics. In Section 3, we examine the existence and stability of steady states as well as investigate local bifurcation scenarios associated with the model. Sections 4 and 5 focus on the stability analysis of diffusion-driven and taxis-driven models, respectively. Numerical simulations are presented in Section 6 to support the analytical results. Lastly, Section 7 discusses the ecological implications of the major findings with relevant ecological examples.

2 Model formulation

Gupta et al. [7] conducted an investigation into a predator–prey model characterized by a constant prey refuge and Holling type II functional response:

$$\begin{aligned}\frac{du}{dt} &= \frac{ru}{1+fv} - r_0u - r_1u^2 - \frac{q\alpha(1-m)uv}{(a+q(1-m)u)}, \\ \frac{dv}{dt} &= sv \left(1 - \frac{\beta v}{q\alpha(1-m)u + (1-q)\alpha_A Q_A} \right),\end{aligned}\tag{1}$$

where u and v denote the quantities of prey and generalist predator species, respectively; r signifies the intrinsic growth rate associated with the prey species; m represents a constant prey refuge constrained within the interval $m \in (0, 1)$; q indicates the predator's preference rate for sustenance, where $q \in (0, 1)$; α is characterized as the maximum rate of prey removal per capita resultant from predation; s denotes the growth rate pertaining

Table 1. Overview of parameters in model (2) and their numerical values for simulations.

Parameter	Description	Units	Value	Source
r	Prey intrinsic growth rate	$(\text{time})^{-1}$	1.6	Assumed
c	Carry-over effect of fear	$(\text{biomass})^{-1}$	0.7	Assumed
f	Cost of fear	$(\text{biomass})^{-1}$	0.9	[7]
r_0	Prey natural death rate	$(\text{time})^{-1}$	0.5	[7]
r_1	Prey intraspecific competition	$(\text{biomass})^{-1}(\text{Time})^{-1}$	0.1	Assumed
q	Predator preference rate	dimensionless	0.63	Assumed
α	Max per capita prey removal	$(\text{time})^{-1}$	0.45	[16]
m	Refuge parameter	dimensionless	0.85	Assumed
a	Half-saturation constant	biomass	0.1	[7]
b	Half-saturation constant	biomass	0.02	Assumed
s	Predator intrinsic growth rate	$(\text{time})^{-1}$	0.05	Assumed
β	Max per capita predator removal	$(\text{time})^{-1}$	0.1	Assumed
α_A	Energy from additional food	$(\text{time})^{-1}$	0.3	[7]
Q_A	Additional food density	biomass	1.8	[7]

to the generalist predator; β represents the maximum rate of predator removal per capita; and α_A along with Q_A account for the decline in predator populations attributable to the availability of its preferred food source and an additional food source maintained at a constant density A . Model (1) has been enhanced through the integration of the following factors:

1. Predators influence prey not only through direct killing but also by inducing fear, which reduces prey reproduction and generates long-term carry-over effects on population density. The prey growth rate is given by $R(c, f, u, v) = (1 + cu)/(1 + cu + fv)$ with properties consistent with [5].
2. Furthermore, the functional response describes the predator’s feeding rate per individual based on prey availability and predator density. Crowley and Martin [3] proposed $P(u, v) = \alpha uv/((1+au)(1+bv))$, where α , a , and b denote capture rate, handling time, and predator interference, respectively. This form is particularly suitable for data with asymptotic feeding rates influenced by predator density.
3. The refuge parameter $m \in (0, 1)$ represents a constant value that denotes the extent of effectiveness of the refuge in preserving prey species. It affords protection to a fraction mu of the prey population, while the remaining $(1 - m)u$ of the prey continue to be vulnerable to predation [8].

Incorporating all the above assumptions, the modified model turns into the following form:

$$\begin{aligned} \frac{du}{dt} &= \frac{ru(1 + cu)}{1 + cu + fv} - r_0u - r_1u^2 - \frac{q\alpha(1 - m)uv}{(1 + a(1 - m)u)(1 + bv)}, \\ \frac{dv}{dt} &= sv \left(1 - \frac{\beta v}{q\alpha(1 - m)u + (1 - q)\alpha_A Q_A} \right), \end{aligned} \tag{2}$$

where $u(0), v(0) \geq 0$, and model parameters are specified in Table 1.

We enhance model (2) by integrating diffusion terms, which facilitates the analysis of both the temporal progression and spatial dynamics associated with species interac-

tions. The incorporation of spatial variations yields a more holistic comprehension of the model's behavior over time and across diverse geographical locations. To further investigate these spatial dynamics, we introduce a self-diffusion term. Self-diffusion signifies the relocation of species within populations, thereby permitting the redistribution from regions of elevated density to areas of diminished density. The subsequent system of parabolic partial differential equations delineates the spatiotemporal dynamics:

$$\begin{aligned}\frac{\partial u}{\partial t} &= ru \left(\frac{1+cu}{1+cu+fv} \right) - r_0u - r_1u^2 - \frac{q\alpha(1-m)uv}{(1+a(1-m)u)(1+bv)} \\ &\quad + \delta_1 \frac{\partial^2 u}{\partial x^2}, \\ \frac{\partial v}{\partial t} &= sv \left(1 - \frac{\beta v}{q\alpha(1-m)u + (1-q)\alpha_A Q_A} \right) + \delta_2 \frac{\partial^2 v}{\partial x^2}.\end{aligned}\quad (3)$$

In this context, the self-diffusion coefficients for prey and predators are denoted by $\delta_1 > 0$ and $\delta_2 > 0$, respectively, thereby encapsulating the intrinsic locomotion patterns exhibited by prey and predators within the spatial domain.

We proceed with the examination of model (3) by taking into account the subsequent initial conditions:

$$u(x, 0) > 0, \quad v(x, 0) > 0, \quad \text{where } x \in \Omega = [0, L], \quad (4)$$

and zero-flux boundary conditions

$$\frac{\partial u}{\partial x} = \frac{\partial v}{\partial x} = 0 \quad \text{on } \partial\Omega. \quad (5)$$

The zero-flux boundary condition (5) implies that no external input is imposed from outside.

The predator's movement in the directed component is governed by prey-taxis, based on the assumption that the acceleration is proportional to the gradient of prey density. The random movement is modeled by a diffusion term. It is assumed that changes in the predator's velocity (acceleration) are influenced by the gradient of prey density, specifically,

$$\left(\frac{\partial}{\partial t} + w \frac{\partial}{\partial x} \right) w = T \frac{\partial u}{\partial x},$$

where the prey-taxis coefficient is represented by $T > 0$, and $w(x, t)$ denotes the predator velocity.

Incorporating diffusion into the velocity equation governing the predator necessitates a modification of the equation as follows:

$$\left(\frac{\partial}{\partial t} + w \frac{\partial}{\partial x} \right) w = T \frac{\partial u}{\partial x} + \delta_3 \frac{\partial^2 w}{\partial x^2},$$

where $\delta_3 > 0$ signifies the diffusion constant associated with the velocity of the predator.

Assuming that the velocity or its gradient is sufficiently small, we are permitted to disregard $w\partial w/\partial x$ in the aforementioned equation, thereby resulting in the subsequent equation:

$$\frac{\partial w}{\partial t} = T \frac{\partial u}{\partial x} + \delta_3 \frac{\partial^2 w}{\partial x^2},$$

where $w(x, t)$ denotes the instantaneous velocity of predator movement at each spatial location [16]. The taxis coefficient T for the prey describes the sensitivity of predator movement to changes in prey density distribution. The parameter δ_3 represents the diffusion coefficient for predator velocity, accounting for the impact of social behavior. Here we have considered a nonstandard prey-taxis formulation by modeling predator velocity (w) as a separate variable influenced by prey density gradients and velocity diffusion. This approach enhances biological realism by capturing gradual predator responses to prey, allows detailed stability analysis, and reveals the role of predator movement in pattern formation. It provides a mechanistic view of how prey-taxis and predator diffusion interact to shape spatiotemporal dynamics.

By incorporating these factors, we propose a prey–predator model with prey-taxis represented by the following reaction–diffusion–advection model:

$$\begin{aligned} \frac{\partial u}{\partial t} &= ru \left(\frac{1 + cu}{1 + cu + fv} \right) - r_0 u - r_1 u^2 - \frac{q\alpha(1 - m)uv}{(1 + a(1 - m)u)(1 + bv)} \\ &\quad + \delta_1 \frac{\partial^2 u}{\partial x^2}, \\ \frac{\partial v}{\partial t} &= sv \left(1 - \frac{\beta v}{q\alpha(1 - m)u + (1 - q)\alpha_A Q_A} \right) - \frac{\partial}{\partial x}(vw) + \delta_2 \frac{\partial^2 v}{\partial x^2}, \\ \frac{\partial w}{\partial t} &= T \frac{\partial u}{\partial x} + \delta_3 \frac{\partial^2 w}{\partial x^2} \end{aligned} \quad (6)$$

with zero-flux boundary conditions

$$w = \frac{\partial u}{\partial x} = \frac{\partial v}{\partial x} = 0 \quad \text{on } \partial\Omega. \quad (7)$$

3 Dynamic behavior of the temporal model

3.1 Positivity and boundedness

Lemma 1. *If $u(0) \geq 0$ and $v(0) \geq 0$, then all the nonnegative solutions of model (2) lie within the region*

$$\Gamma = \{(u, v) \in \mathbb{R}_+^2 : 0 \leq u(t) \leq \mu, 0 \leq v(t) \leq \nu\},$$

where

$$\mu = \frac{r}{r_1} \quad \text{and} \quad \nu = \frac{q\alpha(1 - m)\mu + (1 - q)\alpha_A Q_A}{\beta}.$$

Proof. The proof of this lemma follows from [5]. □

3.2 Feasibility and stability of model's equilibria

The model equation (2) admits three boundary equilibria: the extinction point $E_0(0, 0)$, the prey-only equilibrium $E_1((r - r_0)/r_1, 0)$, and the predator-only equilibrium $E_2(0, (1 - q)\alpha_A Q_A/\beta)$.

Now a coexistence equilibrium exists only when the nontrivial prey nullcline

$$h_1(u, v) = \frac{r(1 + cu)}{1 + cu + fv} - r_0 - r_1 u - \frac{q\alpha(1 - m)v}{(1 + a(1 - m)u)(1 + bv)} = 0$$

and the nontrivial predator nullcline

$$h_2(u, v) = s \left(1 - \frac{\beta v}{q\alpha(1 - m)u + (1 - q)\alpha_A Q_A} \right) = 0$$

converge within the positive quadrant of the uv -plane. In particular, the coexistence equilibrium is realized at the point, where

$$v^* = \frac{q\alpha(1 - m)u^* + (1 - q)\alpha_A Q_A}{\beta}$$

with u^* , which is a positive solution of the equation

$$A_1 u^{*4} + A_2 u^{*3} + A_3 u^{*2} + A_4 u^* + A_5 = 0 \quad (8)$$

with the coefficients

$$\begin{aligned} A_1 &= \beta r_1 acbq\alpha(1 - m)^2 + r_1 a f b q^2 \alpha^2 (1 - m)^3, \\ A_2 &= \beta r_1 acD_1(1 - m) + bq\alpha\beta(r_0(1 - m)a + r_1)(1 - m) \\ &\quad + r_1 a q\alpha(1 - m)^2(fD_1 + bD_2) + f b q^2 \alpha^2 (r_0(1 - m)a + r_1)(1 - m)^2, \\ A_3 &= D_1 \{ c\beta(r_0(1 - m)a + r_1) + r_1 a(1 - m)D_2 \} + q\alpha(r_0(1 - m)a + r_1) \\ &\quad \times (1 - m)(fD_1 + bD_2) + bq\alpha\beta(r_0c - ra(1 - m))(1 - m) \\ &\quad + q^2 \alpha^2 \beta c(1 - m) + b f q^2 \alpha^2 (1 - m)^2, \\ A_4 &= D_1 D_2 (r_0(1 - m)a + r_1) + \beta D_1 (r_0c - ra(1 - m)) + qc\alpha\beta(1 - m) \\ &\quad \times (\beta + (1 - q)\alpha_A Q_A) + f q^2 \alpha^2 \beta (1 - m)^2 + r_0 f q\alpha(1 - m)D_1 \\ &\quad + r_0 b q\alpha(1 - m)D_1 - r b q\alpha\beta(1 - m), \\ A_5 &= \beta q\alpha D_2(1 - m) + r_0 D_1 D_2 - \beta r D_1, \\ D_1 &= (\beta + b(1 - q)\alpha_A Q_A), \quad D_2 = (\beta + f(1 - q)\alpha_A Q_A). \end{aligned}$$

Due to the complexity of the fourth-degree polynomial, analytical determination of coexistence equilibria is difficult. Using Descartes' rule of signs and the conditions in Table 2, Eq. (8) indicates that model (2) can admit up to three interior equilibria, depending on the signs of A_3 , A_4 , and A_5 , with A_1 and A_2 strictly positive.

Table 2. Various cases demonstrate the utmost number of positive real roots.

Signs of A_i for $i = 3, 4, 5$ (A_3, A_4, A_5)	Number of interior equilibrium (atmost)
$(+, +, +)$	0
$(+, +, -), (-, -, -), (+, -, -)$	1
$(+, -, +), (-, +, +), (-, -, +)$	2
$(-, +, -)$	3

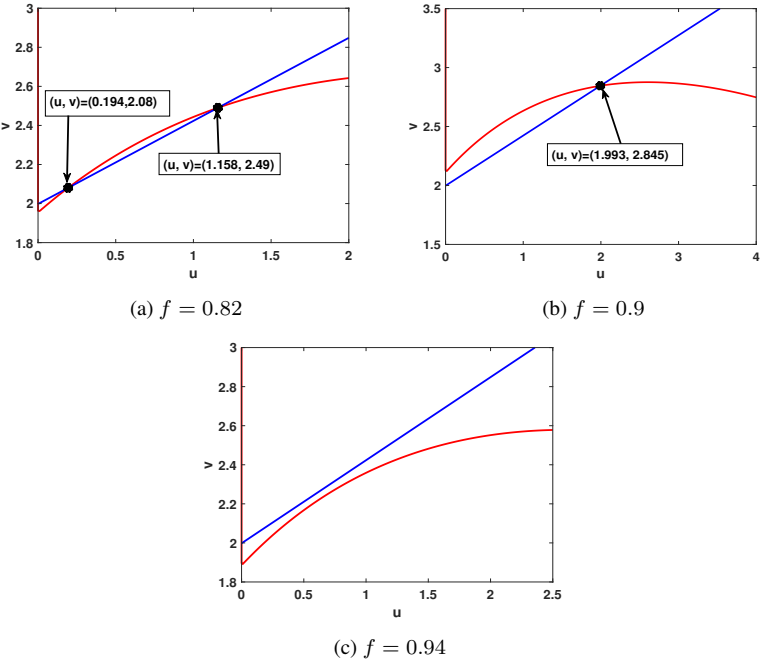


Figure 1. Variation in the number of coexistence equilibrium points for model (2) as the values of f change. The remaining model parameters are specified in Table 1.

Figure 1 illustrates the number of coexistence equilibrium points for model (2) by adjusting significant model parameters using nullcline diagrams.

The Jacobian matrix for model (2) can be written as

$$J(u, v) = \begin{pmatrix} J_{11} & J_{12} \\ J_{21} & J_{22} \end{pmatrix},$$

where

$$J_{11} = \frac{r((1 + cu)^2 + f(1 + 2cu)v)}{(1 + cu + fv)^2} - r_0 - 2r_1u - \frac{q\alpha(1 - m)v}{(1 + bv)(1 + a(1 - m)u)^2},$$
$$J_{12} = -\frac{rf(1 + cu)u}{(1 + cu + fv)^2} - \frac{q\alpha(1 - m)u}{(1 + bv)^2(1 + a(1 - m)u)},$$

$$J_{21} = \frac{s\beta q\alpha(1-m)v^2}{(q\alpha(1-m)u + (1-q)\alpha_A Q_A)^2},$$

$$J_{22} = s \left(1 - \frac{2\beta v}{q\alpha(1-m)u + (1-q)\alpha_A Q_A} \right).$$

At $E_0(0, 0)$, the Jacobian eigenvalues are $\lambda_1 = r - r_0$ and $\lambda_2 = s (> 0)$, implying a saddle for $r < r_0$ and an unstable node for $r > r_0$. At $E_1((r - r_0)r_1, 0)$, the eigenvalues are

$$\lambda_1 = r_0 - r_1, \quad \lambda_2 = s (> 0),$$

so E_1 is a saddle if $r_0 < r_1$ and an unstable node if $r_0 > r_1$.

The eigenvalues associated with the Jacobian matrix evaluated at the equilibrium point $E_2(0, (1 - q)\alpha_A Q_A/\beta)$ are

$$\lambda_1 = \frac{r\beta}{1 + f(1 - q)\alpha_A Q_A} - r_0 - \frac{q\alpha(1 - m)(1 - q)\alpha_A Q_A}{\beta + b(1 - q)\alpha_A Q_A}, \quad \lambda_2 = -s.$$

Thus,

$$E_2 \text{ is } \begin{cases} \text{a stable node} & \text{if } \frac{r\beta}{1 + f(1 - q)\alpha_A Q_A} < r_0 + \frac{q\alpha(1 - m)(1 - q)\alpha_A Q_A}{\beta + b(1 - q)\alpha_A Q_A}, \\ \text{a saddle point} & \text{if } \frac{r\beta}{1 + f(1 - q)\alpha_A Q_A} > r_0 + \frac{q\alpha(1 - m)(1 - q)\alpha_A Q_A}{\beta + b(1 - q)\alpha_A Q_A}. \end{cases}$$

The characteristic equation associated with the Jacobian matrix obtained at the interior equilibrium point $E^*(u^*, v^*)$ is

$$\lambda^2 - (J_{11}^* + J_{22}^*)\lambda + (J_{11}^* J_{22}^* - J_{12}^* J_{21}^*) = 0. \quad (9)$$

By the Routh–Hurwitz criterion, all roots of (9) have negative real parts if and only if

$$(J_{11}^* + J_{22}^*) < 0 \quad \text{and} \quad (J_{11}^* J_{22}^* - J_{12}^* J_{21}^*) > 0.$$

3.3 Bifurcation analysis

In this segment, we demonstrate that the model delineated by Eq. (2) experiences transcritical, saddle-node, Hopf, and Bogdanov–Takens (BT) bifurcations as the parameters are varied in a suitable manner. The specifics of these bifurcations are elaborated upon in the following discussion.

3.3.1 Transcritical bifurcation

A transcritical bifurcation (TB) transpires when two equilibrium states undergo a reciprocal exchange of stability as a parameter transitions through a critical threshold. In this framework, we delineate the subsequent theorem.

Theorem 1. *Model (2) undergoes a TB around the equilibrium E_2 at the critical value*

$$f = f^{\text{TB}} = \frac{(r\beta - r_0)(\beta + b(1 - q)\alpha_A Q_A) - q\alpha(1 - m)(1 - q)\alpha_A Q_A}{(1 - q)\alpha_A Q_A \{r_0(\beta + b(1 - q)\alpha_A Q_A + q\alpha(1 - m)(1 - q)\alpha_A Q_A)\}}$$

if

$$r\beta(\beta + b(1 - q)\alpha_A Q_A) > r_0(\beta + b(1 - q)\alpha_A Q_A) + q\alpha(1 - m)(1 - q)\alpha_A Q_A.$$

Proof. For the manifestation of TB, it is a requisite that one of the eigenvalues of the variational matrix $J(E_2; f = f^{\text{TB}})$ be equal to zero. The variational matrix $J(E_2; f = f^{\text{TB}})$ and its transpose exhibit the respective eigenvectors $G = (1, q\alpha(1 - m)/\beta)^T$ and $H = (1, 0)^T$, which are associated with the zero eigenvalue. In this context, we will elucidate that model (2) attains the state of TB by employing Sotomayor's theorem. We derive the following:

$$\begin{aligned} H^T [F_f(E_2; f = f^{\text{TB}})] &= 0, \\ H^T [DF_f(E_2; f = f^{\text{TB}})G] &= -\frac{r\beta(1 - q)\alpha_A Q_A}{(\beta + f^{\text{TB}}(1 - q)\alpha_A Q_A)^2} \neq 0, \\ H^T [D^2 F(E_2; f = f^{\text{TB}})(G, G)] &= \frac{2rcf^{\text{TB}}\beta(1 - q)\alpha_A Q_A}{D_2^2} \\ &\quad - 2r_1 - \frac{2qa\alpha(1 - m)^2(1 - q)\alpha_A Q_A}{D_1} \\ &\quad + \frac{q^2\alpha^2\beta(1 - m)^2}{D_1^2} - \frac{rqf^{\text{TB}}\alpha\beta(1 - m)}{D_2} \\ &\neq 0. \end{aligned}$$

Therefore, at the instant when the variable f reaches the pivotal threshold f^{TB} , the model delineated by (2) undergoes a transcritical bifurcation that arises from the equilibrium state E_2 . \square

3.3.2 Saddle-node bifurcation

In the context of dynamic models, a saddle-node bifurcation transpires when a pair of equilibrium points collide and subsequently vanish. This occurrence manifests within autonomous models governed by ordinary differential equations when the eigenvalues associated with the Jacobian matrix of the model at the critical juncture tend toward zero.

Theorem 2. *Model (2) displays a saddle-node (SN) bifurcation at the coexistence equilibrium point E^* as c reaches a threshold value $c = c^{\text{SN}}$.*

Proof. Model (2) can also be written as

$$\frac{dP}{dt} = F = [F_1(P, c) \ F_2(P, c)]^T,$$

where $P = [u \ v]^T$, and

$$\begin{aligned} F_1(P, c) &= \frac{ru(1 + cu)}{1 + cu + fv} - r_0u - r_1u^2 - \frac{q\alpha(1 - m)uv}{(1 + a(1 - m)u)(1 + bv)}, \\ F_2(P, c) &= sv \left(1 - \frac{\beta v}{q\alpha(1 - m)u + (1 - q)\alpha_A Q_A} \right). \end{aligned}$$

Now, we derive the necessary transversality conditions that must be satisfied for the realization of saddle-node bifurcation at the critical parameter value $c = c^{\text{SN}}$. The pivotal parameter value of c can be deduced from the stability criterion pertaining to the equilibrium point E^* as $c = c^{\text{SN}}$. At the threshold $c = c^{\text{SN}}$, it is evident that the Jacobian matrix $J(E^*)$ possesses a zero eigenvalue. The eigenvectors corresponding to the Jacobian matrices $J(E^*; c = c^{\text{SN}})$ and $J(E^*; c = c^{\text{SN}})^T$ that are associated with the zero eigenvalue are delineated as follows:

$$V = \begin{pmatrix} V_1 \\ V_2 \end{pmatrix}, \quad W = \begin{pmatrix} W_1 \\ W_2 \end{pmatrix}.$$

Here $V_1 = -J_{12}^* V_2 / J_{11}^* = -J_{22}^* V_2 / J_{21}^*$, $W_1 = -J_{21}^* W_2 / J_{11}^* = -J_{22}^* W_2 / J_{12}^*$ as $V_2 \neq 0$ and $W_2 \neq 0$. Next, the following will be computed using the above values:

$$W^T F_c(E^*; c = c^{\text{SN}}) = \begin{pmatrix} W_1 \\ W_2 \end{pmatrix}^T \left(\begin{array}{c} \frac{rfu^{*2}v^*}{(1+c^{\text{SN}}u^*+fv^*)^2} \\ 0 \end{array} \right) \Bigg|_{(E^*; c=c^{\text{SN}})} \neq 0,$$

$$D^2 F(E^*; c = c^{\text{SN}})(V, V) = \left(\begin{array}{c} \frac{\partial^2 F_1}{\partial u^2} V_1^2 + 2 \frac{\partial^2 F_1}{\partial u \partial v} V_1 V_2 + \frac{\partial^2 F_1}{\partial v^2} V_2^2 \\ \frac{\partial^2 F_2}{\partial u^2} V_1^2 + 2 \frac{\partial^2 F_2}{\partial u \partial v} V_1 V_2 + \frac{\partial^2 F_2}{\partial v^2} V_2^2 \end{array} \right) \Bigg|_{(E^*; c=c^{\text{SN}})} \neq 0.$$

Thus,

$$W^T [F_c(E^*; c = c^{\text{SN}})] \neq 0, \quad W^T [D^2 F(E^*; c = c^{\text{SN}})(V, V)] \neq 0.$$

The analysis reveals that the model defined by Eq. (2) experiences a saddle-node bifurcation at the critical parameter value $c = c^{\text{SN}}$. At this threshold, the equilibrium state E^* shifts as c crosses its critical value. \square

3.3.3 Hopf bifurcation

It has been demonstrated that the stability of E^* is contingent upon the sign of $\text{Tr}(J(E^*))$. In this context, let us define f as a bifurcation parameter. The equilibrium point E^* experiences a loss of stability when the sign of $\text{Tr}(J(E^*))$ transitions from negative to positive due to variations in f . By resolving the equation $\text{Tr}(J(E^*)) = 0$, we derive

$$f = -\frac{(2\tilde{A}(1+cu^*)+rcu^*)+\sqrt{4\tilde{A}(1+cu^*)rcu^*+c^2r^2u^{*2}}}{2\tilde{A}v^*},$$

where

$$\tilde{A} = \frac{qa\alpha(1-m)^2u^*v^*}{(1+a(1-m)u^*)^2(1+bv^*)} - r_1u^* - \frac{s\beta v^*}{q\alpha(1-m)u^*+(1-q)\alpha_A Q_A}.$$

This constitutes an implicit formulation for f as the variables (u^*, v^*) are contingent upon f . We represent the solution of this implicit formulation as f^{H} . The coexisting equilibrium E^* of the model defined by (2) experiences a Hopf bifurcation when $f = f^{\text{H}}$, provided that the subsequent nonhyperbolicity and transversality conditions are met:

$$\text{Det}(J_{E^*}; f = f^{\text{H}}) > 0, \quad \frac{d(\text{Tr}(J_{E^*}))}{df} \Bigg|_{f=f^{\text{H}}} = \frac{rc(1+cu^*-f^{\text{H}}v^*)u^*v^*}{(1+cu^*+f^{\text{H}}v^*)^3} \neq 0.$$

3.3.4 Bogdanov–Takens bifurcation

Theorem 3. *Model (2) undergoes codimension-2 BT bifurcation with respect to fear parameter f and carry-over parameter c at $f = f^{\text{BT}}$ and $c = c^{\text{BT}}$ around the interior equilibrium $E^*(u^*, v^*)$.*

Proof. For brevity, the proof of the theorem is omitted. Interested readers can refer to [18] for details. \square

4 Analysis of diffusion driven model

In this segment, we conduct an examination of the stability characteristics of model (3) under the initial condition (4) and the boundary condition (5). The objective of this section is to explore the ramifications of diffusion on the equilibrium steady state. Furthermore, we concentrate on the scenarios that may potentially lead to Turing instability.

4.1 Stability of steady state

In the context of diffusion phenomena, let us define $u = \bar{u}^* + \bar{U}$ and $v = \bar{v}^* + \bar{V}$, where $|\bar{U}|$ and $|\bar{V}|$ are significantly less than one. To investigate the model delineated in (3), we shall conduct an analysis of the linearized model, which can be expressed as

$$\frac{\partial \bar{U}}{\partial t} = C_{11}\bar{U} + C_{12}\bar{V} + \delta_1 \frac{\partial^2 \bar{U}}{\partial x^2}, \quad \frac{\partial \bar{V}}{\partial t} = C_{21}\bar{U} + C_{22}\bar{V} + \delta_2 \frac{\partial^2 \bar{V}}{\partial x^2}, \quad (10)$$

where the $C_{ij} = J_{ij}$ at point (\bar{u}^*, \bar{v}^*) . Let

$$J_c = \begin{bmatrix} C_{11} & C_{12} \\ C_{21} & C_{22} \end{bmatrix}, \quad \delta = \begin{bmatrix} \delta_1 & 0 \\ 0 & \delta_2 \end{bmatrix}.$$

Let the solution of model (10) be of the form

$$\bar{U} = X e^{\xi_k t} \sin\left(\frac{d\pi}{D}x\right), \quad \bar{V} = Y e^{\xi_k t} \sin\left(\frac{d\pi}{D}x\right). \quad (11)$$

From (10) and (11) we get

$$\frac{\partial \bar{U}}{\partial t} = C_{11}\bar{U} + C_{12}\bar{V} - \delta_1 k^2 \bar{U}, \quad \frac{\partial \bar{V}}{\partial t} = C_{21}\bar{U} + C_{22}\bar{V} - \delta_2 k^2 \bar{V},$$

where $k^2 = (d\pi/D)^2$. The Jacobian matrix corresponding to the aforementioned system is expressed as follows:

$$N^* = \begin{bmatrix} n_{11} & n_{12} \\ n_{21} & n_{22} \end{bmatrix} = \begin{bmatrix} C_{11} - \delta_1 k^2 & C_{12} \\ C_{21} & C_{22} - \delta_2 k^2 \end{bmatrix}.$$

The defining equation associated with the Jacobian matrix N^* can be articulated in the following manner:

$$\xi_k^2 - \text{Tr}(N^*)\xi_k + \text{Det}(N^*) = 0.$$

Applying the Routh–Hurwitz criteria, we determine that the perturbation becomes unstable if any of the conditions below holds:

$$\text{Tr}(N^*) > 0, \quad (12)$$

$$\text{Det}(N^*) < 0. \quad (13)$$

Since $\delta_1, \delta_2 > 0$ and $\text{Tr}(J) < 0$, condition (12) can never be met. However, condition (13) may still hold, which is precisely the criterion for Turing instability. Therefore, by simplifying Eq. (13), we derive the following theorem characterizing Turing instability.

Theorem 4. *The prerequisites for the emergence of Turing instability, instigated by the phenomenon of self-diffusion, for the mathematical model represented by Eq. (3) are:*

- (i) $C_{11} + C_{22} < 0$;
- (ii) $C_{11}C_{22} - C_{12}C_{21} > 0$;
- (iii) $\delta_1 C_{22} + \delta_2 C_{11} > 0$;
- (iv) $(\delta_1 C_{22} + \delta_2 C_{11})^2 > 4 \text{Det}(J_c) \delta_1 \delta_2$.

5 Stability analysis of taxis-driven model

In this segment, we undertake a comprehensive stability analysis of the model delineated in (6), taking into account the specified boundary condition articulated in (7).

We have examined the linearized representation of model (6) around the equilibrium point $E^*(\bar{u}^*, \bar{v}^*, 0)$, incorporating minor perturbations $\bar{U}(x, y, t)$, $\bar{V}(x, y, t)$, and $\bar{W}(x, y, t)$ as follows:

$$\begin{aligned} \frac{\partial \bar{U}}{\partial t} &= C_{11} \bar{U} + C_{12} \bar{V} + \delta_1 \frac{\partial^2 \bar{U}}{\partial x^2}, \\ \frac{\partial \bar{V}}{\partial t} &= C_{21} \bar{U} + C_{22} \bar{V} + \bar{v}^* \frac{\partial \bar{W}}{\partial x} + \delta_2 \frac{\partial^2 \bar{V}}{\partial x^2}, \\ \frac{\partial \bar{W}}{\partial t} &= T \frac{\partial \bar{U}}{\partial x} + \delta_3 \frac{\partial^2 \bar{W}}{\partial x^2}. \end{aligned} \quad (14)$$

Let us postulate the Fourier series solutions corresponding to model (14) in the following manner:

$$\begin{aligned} U(x, y, t) &= \sum_{\eta} U_{\eta} e^{\lambda_{\eta} t} \cos(\eta x), \\ V(x, y, t) &= \sum_{\eta} V_{\eta} e^{\lambda_{\eta} t} \cos(\eta x), \\ W(x, y, t) &= \sum_{\eta} W_{\eta} e^{\lambda_{\eta} t} \sin(\eta x), \end{aligned}$$

where $\eta = d\pi/D$.

Incorporating these parameters into model (14) results in the transformation of the equation into

$$\begin{aligned} \sum_{\eta} U_{\eta} (C_{11} - \lambda_{\eta} - \delta_1 \eta^2) + \sum_{\eta} V_{\eta} C_{12} &= 0, \\ \sum_{\eta} U_{\eta} C_{21} + \sum_{\eta} V_{\eta} (C_{22} - \lambda_{\eta} - \delta_2 \eta^2) - \sum_{\eta} W_{\eta} (v^* \eta) &= 0, \\ \sum_{\eta} U_{\eta} (-T \eta) + \sum_{\eta} (-\delta_3 \eta^2 - \lambda_{\eta}) &= 0. \end{aligned} \quad (15)$$

The Jacobian matrix corresponding to the aforementioned model (15) is articulated as follows:

$$M^* = \begin{bmatrix} C_{11} - \delta_1 \eta^2 & C_{12} & 0 \\ C_{21} & C_{22} - \delta_2 \eta^2 & -v^* \eta \\ -T \eta & 0 & -\delta_3 \eta^2 \end{bmatrix}.$$

The characteristic equation of the above matrix is given by

$$\lambda_{\eta}^3 + p_1 \lambda_{\eta}^2 + p_2 \lambda_{\eta} + p_3 = 0,$$

where

$$\begin{aligned} p_1 &= \eta^2 (\delta_1 + \delta_2 + \delta_3) - (C_{11} + C_{22}), \\ p_2 &= \eta^4 (\delta_1 \delta_2 + \delta_2 \delta_3 + \delta_3 \delta_1) \\ &\quad - \eta^2 (C_{11} \delta_2 + C_{22} \delta_1 + C_{11} \delta_3 + C_{22} \delta_3) \\ &\quad + (C_{11} C_{22} - C_{12} C_{21}), \\ p_3 &= \eta^2 (\delta_1 \delta_2 \delta_3 \eta^4 - C_{11} \delta_2 \delta_3 \eta^2 - C_{12} C_{21} \delta_3 - C_{12} v^* T). \end{aligned}$$

Through the application of the Routh–Hurwitz criteria, it is determined that local asymptotic stability is attained at the positive equilibrium point $E^*(\bar{u}^*, \bar{v}^*, 0)$ if and only if

$$p_1 > 0 \quad p_3 > 0, \quad \text{and} \quad p_1 p_2 - p_3 > 0.$$

6 Computational results

This section presents the numerical computation of the analytical findings. Comprehensive numerical simulations were executed employing MATLAB R2024a, MAPLE 16, and MATHEMATICA software to corroborate the theoretical findings. The parameters selected for the validation of the analytical results are enumerated in Table 1.

6.1 Computational results for temporal model

6.1.1 Bifurcation structure with varying levels of predator-induced fear f

The parameter f (predator-induced fear) is the primary bifurcation parameter driving system dynamics. For $f \leq 0.852969$, the model admits a stable coexistence equilibrium,

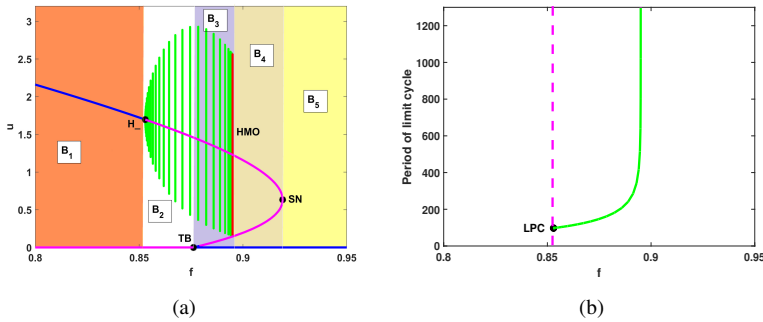


Figure 2. One-parameter bifurcation analysis of the model described in Eq. (2), focusing on how variations in the fear parameter f affect the system’s equilibrium states and dynamic transitions. In this figure, HMO denotes a homoclinic orbit associated with abrupt changes in population levels, SN indicates a saddle-node bifurcation, where equilibrium points merge or disappear, and H_- represents a supercritical Hopf bifurcation where a stable steady state gives rise to stable oscillatory behavior. The magenta lines correspond to branches of unstable equilibrium points, while the blue lines indicate stable equilibrium branches.

but at $f = 0.852969$ a Hopf bifurcation produces stable limit cycles around E^* . Within $0.852969 < f < 0.876155$, these cycles remain stable, while a transcritical bifurcation at $f^{TB} = 0.876155$ introduces bistability between the prey-free state and the limit cycle. As f increases further, cycle amplitudes grow until a homoclinic bifurcation occurs at $f = 0.88$, followed by extinction of coexistence equilibria through a saddle-node bifurcation at $f = 0.919135$. Beyond this point ($f \geq 0.919135$), only the prey-free state persists. The period analysis (Fig. 2(b)) shows an increasing trend as f approaches 0.88. Ecologically, this suggests that as predator-induced fear intensifies, it can significantly alter prey behavior and reduce their ability to maintain stable populations. High levels of fear can lead to long-term population oscillations or even extinction, emphasizing that fear itself, without direct predation, can act as a powerful force shaping species interactions and overall ecosystem stability.

6.1.2 Bifurcation structure with varying the rate of prey’s carry-over effects c due to predator-induced fear

The stability of equilibrium under varying prey carry-over effects c exhibits rich dynamical behavior. For small c , the system stabilizes at the prey-free equilibrium, while at $c = 0.648253$ a saddle-node bifurcation generates two coexistence equilibria, one stable and one unstable. Within $0.648253 < c < 0.651774$, bistability occurs between the coexistence and prey-free equilibria, followed by a Hopf bifurcation at $c = 0.651774$ that produces stable population cycles. These cycles coexist with the prey-free state until a homoclinic bifurcation near $c = 0.67$ triggers extinction. Between $0.67 < c < 0.74$, further homoclinic transitions alter stability, and for $c > 0.8257$, the cycles vanish via another Hopf bifurcation, leaving bistability between steady states. Period analysis (Fig. 3(b)) confirms that cycle periods initially increase with c before declining beyond $c = 0.74$. Ecologically, this shows that carry-over effects, such as delayed impacts on growth or

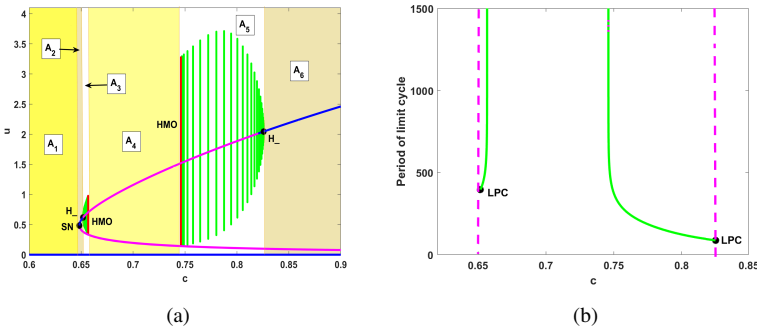


Figure 3. One-parameter bifurcation analysis of the model described in Eq. (2), focusing on how changes in the carry-over effect parameter c influence the system's equilibria and dynamic behavior. In the diagram, HMO indicates the presence of a homoclinic orbit, SN marks the location of a saddle-node bifurcation, and H_- denotes a supercritical Hopf bifurcation point where stable steady states give rise to stable oscillatory solutions. The magenta lines represent branches of unstable equilibrium points, while the blue lines correspond to stable equilibrium branches.

reproduction, can have lasting consequences on prey populations. As these effects become stronger, they can disrupt population balance and lead to sudden shifts in dynamics, highlighting the importance of long-term stress responses in ecosystem stability.

6.1.3 The dynamic interaction between the prey's carry-over effects of predator-induced fear and the level of predator-induced fear

In this section, we elucidate the global and local bifurcation outcomes pertinent to model (2), which were derived utilizing the Matlab software package. Figure 4(a) presents a bifurcation diagram within the two-dimensional cf -plane to facilitate enhanced visualization. The local bifurcation trajectories encompass the SN bifurcation curve, the TB curve, and the Hopf bifurcation curve, whereas the global bifurcation trajectory comprises the homoclinic curve (HMO). These trajectories segment the cf -plane into seven distinct regions designated as R_1 through R_7 . In accordance with Theorem 1, the trivial equilibrium E_0 is characterized as unstable, while the axial equilibrium point E_1 is consistently a saddle across all delineated regions. Conversely, the alternative axial equilibrium point, E_2 , is identified as a saddle within regions R_5 and R_6 , yet exhibits stability in the remaining regions. We now scrutinize the dynamics of the interior equilibrium points of model (2) across each region, as well as the alterations in dynamical behavior as they pertain to the bifurcation curves. The dynamic behaviors observed in each region are comprehensively summarized in Table 3, and schematic phase portraits illustrating the coexisting equilibria in each region are represented in Figs. 5, 6 for enhanced clarity. Furthermore, we note that the saddle-node curve intersects with the Hopf curve at a BT point ($c^{\text{BT}} = 0.672323$ and $f^{\text{BT}} = 0.908442$), which signifies a codimension-2 bifurcation. At the coordinates $c = 1.12007$ and $f = 1.05241$, the model demonstrates a generalized Hopf (GH) bifurcation, wherein the first Lyapunov coefficient attains a value of zero, and two limit cycles are observed surrounding the equilibrium point E^* (2.457392, 3.043006).

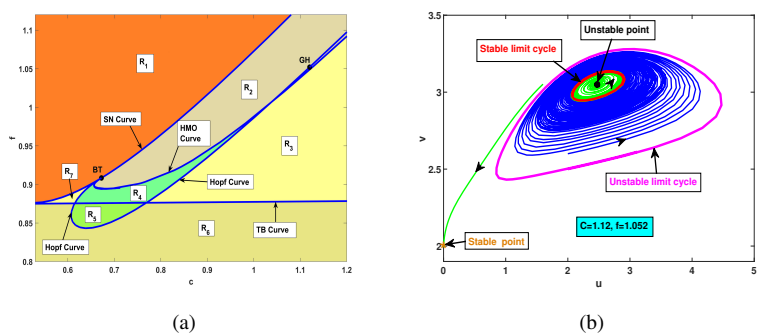


Figure 4. Bifurcation diagrams for model (2) in the two-dimensional cf -plane with all other parameters fixed as given in Table 1. The diagram divides the plane into seven regions (R_1 – R_7) delineated by local bifurcation curves – SN, TB, and Hopf bifurcation curves – as well as the global HMO curve. A summary of the stability properties and bifurcation-induced regime shifts in each region is provided in Table 3.

Table 3. Nature of equilibrium points of model (2) in different regions of Fig. 4; SP (stable-node), UN (unstable-node), SN (saddle-node), and SF (stable-focus).

Region	Equilibrium point(s)	Nature of equilibria	Phase portrait
R_1	E_0, E_1, E_2	UN, SN, SP	Fig. 5(a)
R_2	$E_0, E_1, E_2, E_1^*, E_2^*$	UN, SN, SP, SN, SN	Fig. 5(b)
R_3	$E_0, E_1, E_2, E_1^*, E_2^*$	UN, SN, SP, SN, SP	Fig. 6(a)
R_4	$E_0, E_1, E_2, E_1^*, E_2^*$	UN, SN, SP, SN, SF	Fig. 6(b)
R_5	E_0, E_1, E_2, E^*	UN, SN, SN, SF	Fig. 6(c)
R_6	E_0, E_1, E_2, E^*	UN, SN, SN, SP	Fig. 6(d)
R_7	$E_0, E_1, E_2, E_1^*, E_2^*$	UN, SN, SP, SN, SP	Fig. 6(e)

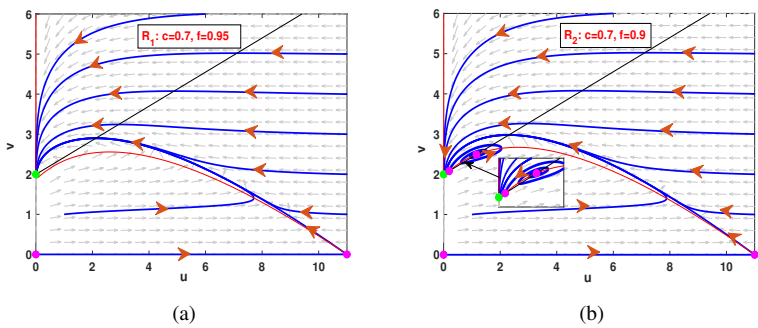


Figure 5. Phase portraits of model 2 for regions R_1 – R_2 (Fig. 4) using parameters from Table 1. Trajectories (blue) and separatrices (cyan) depict solution paths; the prey and predator nullclines are represented by red and black curves, respectively. Stable (green) and unstable (magenta) equilibria govern the dynamics.

(as illustrated in Fig. 4(b)). A subcritical Hopf bifurcation is noted to occur to the right of the GH point, while a supercritical Hopf bifurcation is observed to the left of the GH point.

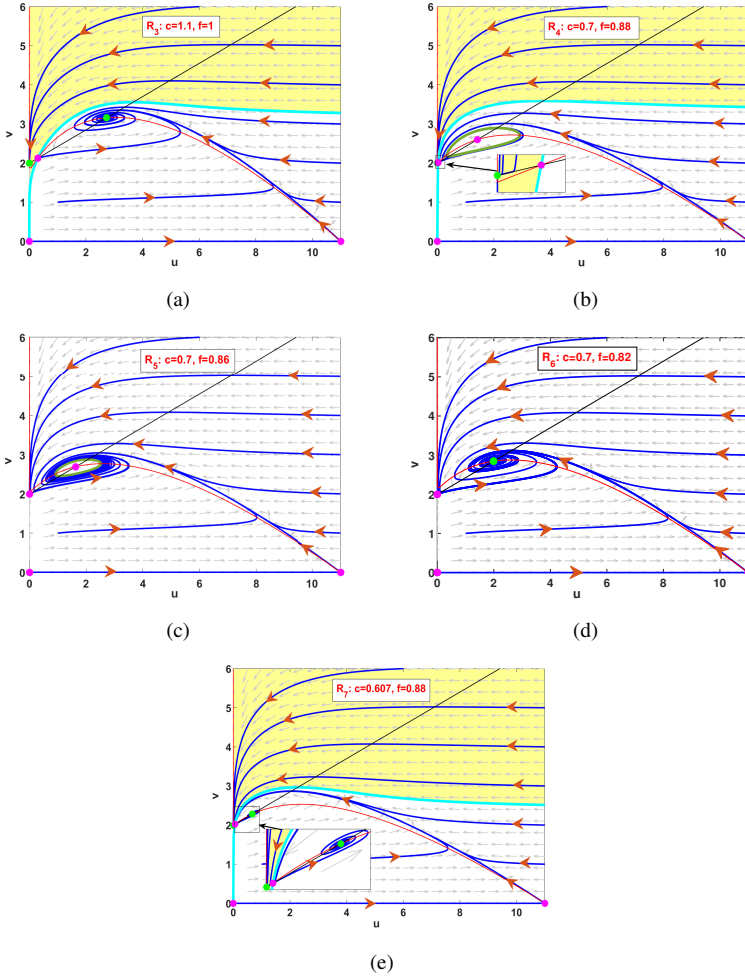


Figure 6. Phase portraits of model 2 for regions R_3 – R_7 (Fig. 4) using parameters from Table 1. Trajectories (blue) and separatrices (cyan) depict solution paths; the prey and predator nullclines are represented by red and black curves, respectively. Stable (green) and unstable (magenta) equilibria govern the dynamics.

6.2 Computational results for reaction–diffusion and reaction–diffusion–advection equation: Turing pattern formation

To obtain the Turing pattern for models (3) and (6), numerical simulations were performed using MATLAB R2024a. The models were initially discretized by mapping u to (u_0, u_1, \dots, u_N) and v to (v_0, v_1, \dots, v_N) , where $N = 80$. Here we have taken mesh size $h = 0.3$ and time $t = 70000$. The simulation parameters were then established as follows.

For the diffusion-driven pattern formation,

$$r = 1.6, \quad c = 0.7, \quad f = 0.9, \quad r_0 = 0.5, \quad r_1 = 0.1, \quad m = 0.8631, \quad (16_1)$$

$$\begin{aligned} q = 0.63, \quad a = 0.1, \quad b = 0.02, \quad s = 0.05, \quad \beta = 0.1, \\ \alpha = 0.45, \quad \alpha_A = 0.3, \quad Q_A = 1.8, \quad \delta_1 = 0.03, \quad \delta_2 = 1.2; \end{aligned} \quad (16_2)$$

for the taxis-driven pattern formation,

$$\begin{aligned} r = 1.6, \quad c = 0.7, \quad f = 0.9, \quad r_0 = 0.5, \quad r_1 = 0.1, \quad m = 0.8631, \\ q = 0.63, \quad a = 0.1, \quad b = 0.02, \quad s = 0.05, \quad \beta = 0.1, \quad \alpha = 0.45, \\ \alpha_A = 0.3, \quad Q_A = 1.8, \quad T = 0.3, \quad \delta_1 = 0.03, \quad \delta_2 = 1.2, \quad \delta_3 = 1. \end{aligned} \quad (17)$$

The computational analysis of models (3) and (6) involves using the finite difference method to identify spatiotemporal patterns within a two-dimensional spatial region. The reaction and velocity component is handled using the forward Euler method, diffusion is approximated using the standard central-difference scheme with zero-flux boundary conditions.

The emergence of Turing patterns for various values of t , δ_2 , and T is illustrated in Figs. 7, 8, and 9, respectively. Regions of low prey population density are represented by blue spots, while areas of high population density are shown as red spots.

6.3 Diffusion driven Turing patterns

Given the existence of a one-to-one correspondence between the spatial distributions of both prey and predator species, we have exclusively presented the distributions pertaining to the prey species. The predator patterns follow a similar structure due to their strong coupling in the reaction–diffusion model.

Figure 7 illustrates the development of Turing patterns as the time t is varied. As t increases, the regular stripe-shaped patterns emerge and progressively occupy the entire bounded domain. These patterns grow faster over time, reflecting the model's dynamic evolution.

In Fig. 8, we illustrate the development of Turing patterns as the predator self-diffusion coefficient, δ_2 , is varied. At lower values of δ_2 , irregularly shaped hot spots dominate areas where prey density is lower. As δ_2 increases, these hot spots gradually transform into irregular stripes, leading to a reduction in the overall prey population. When δ_2 reaches sufficiently high levels, the irregular stripes stabilize into regular, well-defined stripes.

6.4 Taxis driven Turing patterns

The examination of the model through simulation within a heterogeneous environment demonstrates that both prey-taxis and the random movement of predators profoundly affect the spatial distribution of various species. Prey-taxis, where predators move toward higher prey density, leads to a more organized and directed predator–prey interaction, while the random movement of predators introduces variability in their positioning. Together, these dynamics shape the formation of spatial patterns and influence the overall stability and coexistence of species within the ecosystem.

In Fig. 9, Turing patterns are displayed for the predator species and predator velocity as the prey-taxis parameter T is varied. It is evident from the patterns of the predators

that increasing T causes the irregularly shaped unstable stripes to evolve into cold spots surrounded by highly dense stripes. These cold spots gradually become more stable wave-type patterns with the further increase. We can also notice from the patterns of predator velocity that as prey-taxis T intensifies, predators are more strongly attracted to areas of high prey density, causing an increase in their velocity. This means predators will move more rapidly toward regions where prey populations are abundant.

7 Conclusion

In this article, we examined a generalist predator–prey model that integrates the concept of predator-induced fear alongside its consequential carry-over effects. The functional response within the prey equation is conceptualized as a Crowley–Martin type, whereas the growth dynamics of the predator population are regulated through an adapted Leslie–Gower framework. We investigate the temporal and spatiotemporal dynamics across a range of parameter configurations. The analysis uncovers intricate dynamics characterized by bistability and both local as well as global bifurcations, while also assessing how these dynamics fluctuate in relation to varying parameter values within the temporal model.

Our research demonstrates that the fear induced by predators and its subsequent effects exert contrasting influences on the dynamics of the model. From Fig. 3 it is evident that at minimal levels of the carry-over effect, the model maintains stability at an equilibrium devoid of prey, wherein the predator species fails to endure. In scenarios

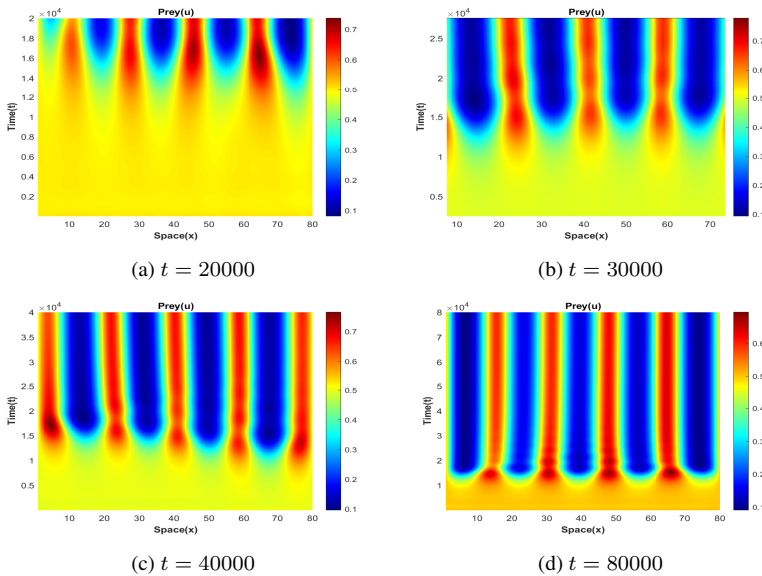


Figure 7. Spatiotemporal evolution of prey density governed by the reaction–diffusion equation (3) at increasing time values with parameters fixed as in Eq. (16).

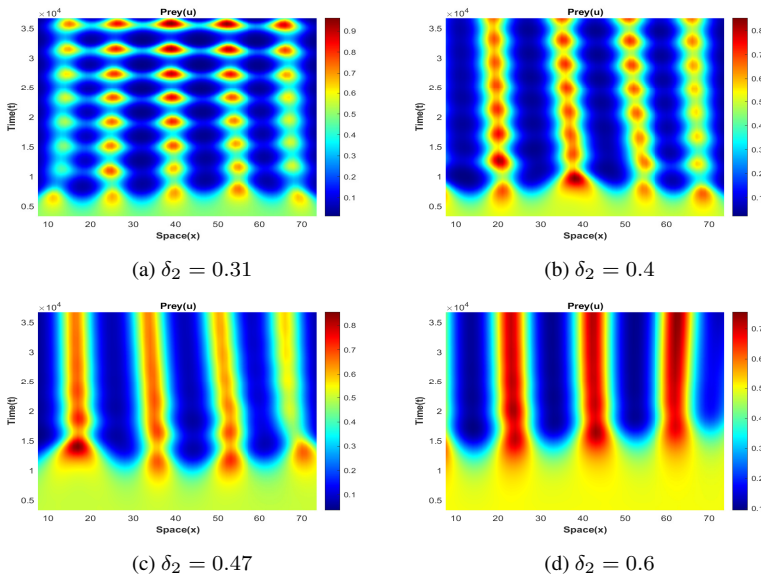


Figure 8. Spatiotemporal patterns of prey density governed by reaction–diffusion equation (3) under varying predator self-diffusion coefficients with other parameters fixed as in Eq. (16).

characterized by intermediate levels, the model manifests periodic oscillations, culminating in a phenomenon of stability-switching facilitated by a Hopf bifurcation. Notably, at elevated levels of the carry-over effect, these oscillations are mitigated, culminating in model stability. A subsequent Hopf bifurcation transpires as the model evolves from a limit cycle to a stable node, thereby illustrating that the carry-over effect ultimately functions as a stabilizing agent. Conversely, as illustrated in Fig. 2, we observe that when the predator-induced fear is markedly low, both populations not only persist but also stabilize within the ecosystem, rendering the prey-free equilibrium point unstable. Nevertheless, an escalation in the fear parameter destabilizes the model, prompting a Hopf bifurcation. This finding implies that predator-induced fear and carry-over effects exhibit diametrically opposed behaviors, thereby influencing the model dynamics in divergent manners. Furthermore, we have investigated codimension-2 bifurcations, such as the BT bifurcation, as depicted in Fig. 4.

Turing instability in reaction–diffusion and reaction–diffusion–advection models explains the spontaneous emergence of spatial patterns, driven by diffusion and taxis processes. Analyzing stability near the interior equilibrium $E(u^*, v^*)$, we observed diverse spatial formations, such as stripes, spots, and holes (Figs. 7–9), reflecting predator–prey interactions under varying self-diffusion and prey-taxis intensities. Figure 9 shows that increasing prey-taxis enhances pattern stability, highlighting its role as a biological control mechanism. Few reaction–diffusion models account for active animal movement, such as foraging optimization, yet both directed and random motions are crucial for population regulation. These findings are comparable to the results given by Gupta et al. [7] where they have investigated complex dynamics of Leslie–Gower prey–predator model with

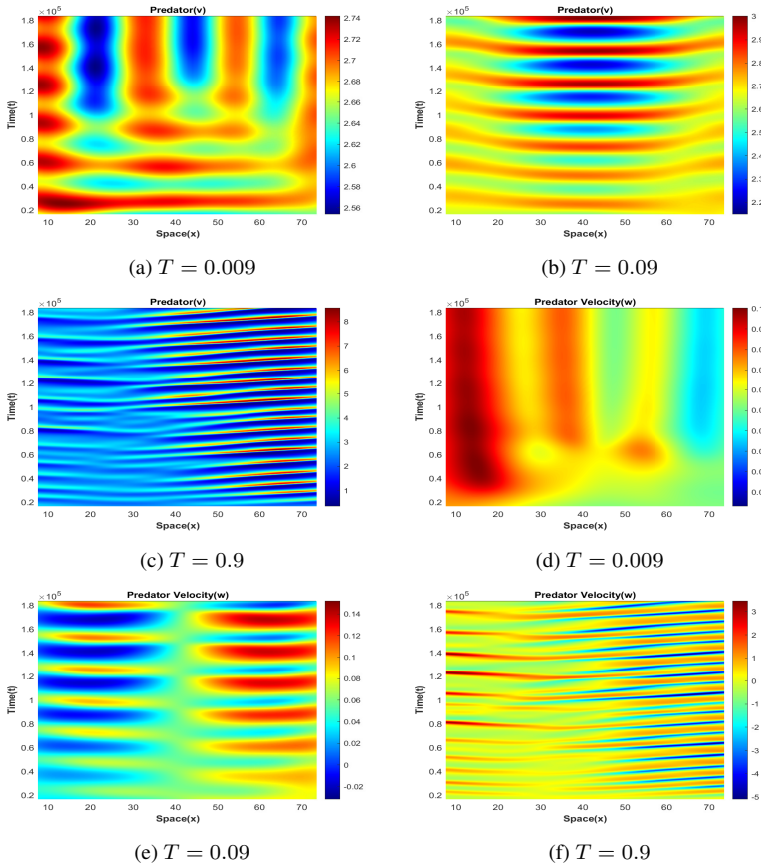


Figure 9. Spatiotemporal patterns of predator density and velocity field governed by the advection–reaction–diffusion system (6) under varying prey–taxi sensitivity with other parameters fixed as in (17).

fear, refuge, and additional food. They analyzed their model in the absence of carry-over effects and predator velocity. In our analysis, we investigated how predator velocity influences pattern formation, aiming to enhance the realism of our study. Rai et al. [16] also investigated the complex dynamics of a one-dimensional spatial nonlinear reaction–diffusion–advection system with a Holling type IV functional response.

A promising avenue for future inquiry may encompass the exploration of the dynamics of our proposed model through the incorporation of a carry-over delay. Additionally, the model could be further enhanced by integrating predator–taxi and prey movement velocity. Investigating these extensions may yield profound insights into the spatiotemporal interactions and pattern formation inherent in prey–predator models. Such advancements could also facilitate a more holistic understanding of ecological responses to environmental and behavioral determinants.

Conflicts of interest. The authors declare no conflicts of interest.

Acknowledgment. The authors express their gratitude to the anonymous reviewers whose comments and suggestions have helped the improvements of this paper.

References

1. M.J. Barry, The costs of crest induction for *Daphnia carinata*, *Oecologia*, **97**:278–288, 1994, <https://doi.org/10.1007/BF00323161>.
2. B. Bhunia, T.K. Kar, S. Ghorai, Spatiotemporal flow-induced instability of predator–prey model with Crowley–Martin functional response and prey harvesting, *Chaos*, **34**(8):083139, 2024, <https://doi.org/10.1063/5.0222487>.
3. P.H. Crowley, E.K. Martin, Functional responses and interference within and between year classes of a dragonfly population, *J. N. Am. Benthol. Soc.*, **8**(3):211–221, 1989, <https://doi.org/10.2307/1467324>.
4. M. De Block, R. Stoks, Fitness effects from egg to reproduction: Bridging the life history transition, *Ecology*, **86**(1):185–197, 2005, <https://doi.org/10.1890/04-0116>.
5. B. Dubey, A. Singh, Anshu, Spatiotemporal dynamics of prey–predator model incorporating Holling-type II functional response with fear and its carryover effects, *Chaos*, **34**(5):053108, 2024, <https://doi.org/10.1063/5.0203353>.
6. A. Gierer, H. Meinhardt, A theory of biological pattern formation, *Kybernetik*, **12**:30–39, 1972, <https://doi.org/10.1007/BF00289234>.
7. A. Gupta, A. Kumar, B. Dubey, Complex dynamics of Leslie–Gower prey–predator model with fear, refuge and additional food under multiple delays, *Int. J. Biomath.*, **15**(08):2250060, 2022, <https://doi.org/10.1142/S1793524522500607>.
8. T.K. Kar, Stability analysis of a prey–predator model incorporating a prey refuge, *Commun. Nonlinear Sci. Numer. Simul.*, **10**(6):681–691, 2005, <https://doi.org/10.1016/j.cnsns.2003.08.006>.
9. J. Lee, T. Hillen, M. Lewis, Pattern formation in prey–taxis systems, *J. Biol. Dyn.*, **3**(6):551–573, 2009, <https://doi.org/10.1080/17513750802716112>.
10. H. Malchow, Flow- and locomotion-induced pattern formation in nonlinear population dynamics, *Ecol. Model.*, **82**(3):257–264, 1995, [https://doi.org/10.1016/0304-3800\(94\)00095-Y](https://doi.org/10.1016/0304-3800(94)00095-Y).
11. H. Malchow, Motional instabilities in prey–predator systems, *J. Theor. Biol.*, **204**(4):639–647, 2000, <https://doi.org/10.1006/jtbi.2000.2074>.
12. D.J. Marshall, S.G. Morgan, Ecological and evolutionary consequences of linked life-history stages in the sea, *Curr. Biol.*, **21**(18):R718–R725, 2011, <https://doi.org/10.1016/j.cub.2011.08.022>.
13. A.K. Misra, M. Tiwari, A. Sharma, Spatio-temporal patterns in a cholera transmission model, *J. Biol. Syst.*, **23**(03):471–484, 2015, <https://doi.org/10.1142/S0218339015500242>.
14. C.M. O'Connor, D.R. Norris, G.T. Crossin, S.J. Cooke, Biological carryover effects: Linking common concepts and mechanisms in ecology and evolution, *Ecosphere*, **5**(3):28, 2014, <https://doi.org/10.1890/ES13-00388.1>.

15. E.L. Preisser, D.I. Bolnick, The many faces of fear: Comparing the pathways and impacts of nonconsumptive predator effects on prey populations, *PLoS One*, **3**(6):e2465, 2008, <https://doi.org/10.1371/journal.pone.0002465>.
16. V. Rai, R.K. Upadhyay, N.K. Thakur, Complex population dynamics in heterogeneous environments: Effects of random and directed animal movements, *Int. J. Nonlinear Sci. Numer. Simul.*, **13**(3–4):299–309, 2012, <https://doi.org/10.1515/ijnsns-2011-0115>.
17. D. Sahoo, G.P. Samanta, Impact of fear effect in a two prey-one predator system with switching behaviour in predation, *Differ. Equ. Dyn. Syst.*, **32**(2):377–399, 2024, <https://doi.org/10.1007/s12591-021-00575-7>.
18. A. Singh, A. Kumar, A. Gupta, B. Dubey, Bifurcation and chaos in a diffusive prey–predator model incorporating fear effect on prey and team hunting by predator with anti-predation response delay, *Int. J. Bifurcation Chaos Appl. Sci. Eng.*, **35**(02):2550018, 2025, <https://doi.org/10.1142/S021812742550018X>.
19. A. Stevens, H.G. Othmer, Aggregation, Blowup, and Collapse: The ABC's of Taxis in Reinforced Random Walks, *SIAM J. Appl. Math.*, **57**(4):1044–1081, 1997, <https://doi.org/10.1137/S0036139995288976>.
20. A.M. Turing, The chemical basis of morphogenesis, *Bull. Math. Biol.*, **52**:153–197, 1990, <https://doi.org/10.1007/BF02459572>.
21. X. Wang, L. Zanette, X. Zou, Modelling the fear effect in predator-prey interactions, *J. Math. Biol.*, **73**:1179–1204, 2016, <https://doi.org/10.1007/s00285-016-0989-1>.
22. L.Y. Zanette, A.F. White, M.C. Allen, M. Clinchy, Perceived predation risk reduces the number of offspring songbirds produce per year, *Science*, **334**(6061):1398–1401, 2011, <https://doi.org/10.1126/science.1210908>.